nature communications

Article

https://doi.org/10.1038/s41467-025-66699-4

A hierarchy of time constants and reliable signal propagation in the marmoset cerebral cortex

Received: 28 February 2025

Accepted: 12 November 2025

Published online: 26 November 2025

Check for updates

Guanchun Li[1,4], Songting Li[2] ✉ & Xiao-Jing Wang[3] ✉

A hierarchy of timescales in the cerebral cortex is functionally desirable for rapid information processing in sensory areas and slow time integration in association areas. Here, through an analysis of electrocorticography (ECoG) data, we identified a timescale hierarchy in the neocortex of marmoset, a primate species commonly used in neuroscience. Constrained by the anatomical and electrophysiological data, we developed a multi-regional model of the marmoset neocortex that captures the observed timescale hierarchy phenomenon. Furthermore, we used the model to investigate how the neocortex reconciles information integration on distinct timescales in local areas with reliable signal propagation globally across regions. We found that a near-criticality state is optimal for both localized signal integration within areas and reliable signal propagation across areas in the multi-regional neocortex. Our model also mechanically explains recent experimental observations that the structural and functional connectivities are less correlated in association areas than in sensory areas.

The cerebral cortex, together with peripheral sensory organs (e.g., retina, cochlea, spinal cord) and subcortical relays (e.g., thalamus), engages in information processing of external inputs, local integration of signals within regions, and the transmission of these signals along functionally specific pathways. A prominent and noteworthy characteristic of the neocortex is what is referred to as "timescale hierarchy". In essence, different cortical areas exhibit varying timescales in their response to inputs, allowing for the hierarchical processing of temporal information. Primary sensory areas manifest shorter timescales, typically measured in tens of milliseconds. The short timescales enable these areas to respond rapidly and effectively to incoming stimuli. In contrast, higher-level association areas display longer timescales, often extending to hundreds of milliseconds or longer. These extended timescales support the integration of information over a relatively protracted time window. The phenomenon of timescale hierarchy emerges from a theoretical model of the multi-regional macaque neocortex[1], and is supported by experimental studies conducted on multiple species, including mice[2,3], macaque monkeys[4,5], and humans[6–11]. It remains to be actively investigated on the universality of this phenomenon across different species and the corresponding large-scale circuit mechanisms.

Timescale hierarchy is a phenomenon that spans across multiple cortical areas, strongly suggesting that its underlying mechanism is intricately linked to the broad-scale structural attributes of the neocortex. On an intuitive level, the timescale of neuronal population activity is intricately tied to the strength of recurrent excitation within that population. In simpler terms, stronger recurrent excitation tends to result in slower timescales of activity. Consequently, the concept of timescale hierarchy points to the existence of a macroscopic gradient in recurrent excitation along the axis of cortical area hierarchy. This notion finds compelling support in experimental findings, particularly in studies that examine the number of dendritic spines on pyramidal neurons within the primate neocortex. These dendritic spines serve as a direct reflection of the synaptic excitation strength per neuron and notably display an increasing gradient along the cortical hierarchy[12,13]. Furthermore, beyond this spatial gradient in spine numbers, the

[1]Courant Institute, New York University, New York, NY, USA. [2]School of Mathematical Sciences, MOE-LSC, and Institute of Natural Sciences, Shanghai Jiao Tong University, Shanghai, China. [3]Center for Neural Science, New York University, New York, NY, USA. [4]Present address: Howard Hughes Medical Institute, Baylor College of Medicine, Houston, TX, USA. ✉e-mail: songting@sjtu.edu.cn; xjwang@nyu.edu

neocortex also reveals macroscopic gradients in other biological properties, including neuron density[14] and synaptic receptor distribution[15,16]. These gradients may indeed serve as fundamental principles governing the organization of the cerebral cortex on a large scale, as discussed in a comprehensive review[17].

In addition to the inherent characteristics of individual cortical areas, timescale hierarchy may also be attributed to long-range connections among these areas. Recent years have witnessed significant advancements in the quantitative measurement of inter-areal connectivity in various species, including mouse[18–21], macaque[22–24], and marmoset[25,26]. It represents a departure from earlier studies that only provided a coarse assessment of primate connectomes by categorizing connections between area pairs as absent, weak, or strong[27,28]. In contrast, the contemporary connectome offers a more precise and quantitative characterization. The strength of inter-areal connections is characterized using a continuous metric known as the fraction of labeled neurons (FLNs). FLNs measure the relative strength of projections from a particular source area to a specific target area in relation to all source areas projecting to that target area. Such a detailed connectome framework enables the quantitative exploration of the organizational principles governing the cerebral cortex. For instance, one notable observation is that FLNs between two areas exhibit an exponential decay with increasing distance, a phenomenon known as the exponential distance rule[29,30].

By incorporating the macroscopic gradient of excitation and a quantitative weighted and directed connectome of macaque monkey, a comprehensive multi-regional model of 29 areas was developed to qualitatively generate the timescale hierarchy phenomenon[1]. Notably, when the macroscopic gradient of excitation was removed or the connectivity was shuffled, the significance of the timescale hierarchy diminished, or in some instances, completely vanished[1]. To elucidate the underlying principles governing this phenomenon, a rigorous mathematical analysis was conducted to identify the importance of macroscopic gradient of excitation and detailed excitation-inhibition (E-I) balance. The balance condition stipulated that the inter-areal excitatory inputs originating from each source area must balance with the local inhibitory inputs from the target area[31]. As a result, cortical areas exhibited relatively weak effective interactions, leading to the emergence of timescale hierarchy in a densely connected network.

While this detailed balance condition appeared to enhance signal gating, i.e., irrelevant signals are not able to propagate in the detailed balance state, as demonstrated in a computational study[32], it also introduced a challenge: the model struggled to achieve reliable signal propagation, another crucial dynamic property of the large-scale neural circuits. On the other hand, signals experienced significantly less attenuation when they operated within an alternative dynamical regime known as "global balanced amplification"[33]. However, in this regime, the timescale hierarchy phenomenon ceased to exist. The conundrum lies in reconciling both timescale hierarchy and reliable signal propagation within the cerebral cortex. Furthermore, despite the model being informed by anatomical data, it remains unclear to which extent the model accurately captures the timescales of individual areas and the precise properties of signal propagation in a quantitative manner. A challenge stems from the absence of neuronal activity data recorded across multiple areas in the macaque neocortex.

In this study, starting from analyzing the multi-regional electrocorticography (ECoG) recording data of another primate, the marmoset, we investigated two critical aspects within the marmoset neocortex: the timescale hierarchy phenomenon and the property of signal propagation. It is notable that there has been limited prior research reporting the existence of timescale hierarchy in the marmoset neocortex. Consequently, it becomes imperative to explore whether this phenomenon also manifests in the marmoset, thereby testing the hypothesis that timescale hierarchy may serve as a universal principle governing cortical dynamics across different species. In addition, the availability of comprehensive anatomical data[25,26] along with activity data[34] collected from multiple cortical areas within the marmoset neocortex, provides us with an opportunity to develop a biologically realistic large-scale model that encompasses multiple cortical areas. Importantly, and in contrast to previous research, the predictions made by our model regarding the timescales of individual cortical areas and the patterns of signal propagation across multiple areas can be directly validated using experimental activity data. This anatomically and dynamically constrained model empowers us to delve deeply into the role played by the intra-areal heterogeneity (i.e., macroscopic gradient of excitation) and inter-areal connectivity in shaping local signal integration and global signal propagation dynamics within the marmoset neocortex, in particular, leading to a near-critical state of the neocortex. In addition, the model mechanically explains recent experimental observations that the structural connectivity and functional connectivity are less similar in association areas than in sensory areas.

Results

Experimental evidence of timescale hierarchy in the marmoset neocortex

We initiated our investigation with the analysis of an ECoG dataset recorded from an anesthetized marmoset in a previous study[34]. This dataset includes signal measurement from 96 electrodes, broadly placed on the left hemisphere of the marmoset's brain during a state of passive listening (Fig. 1a). To circumvent any potential bias from the auditory stimulus, we selected data recorded prior to any auditory stimulus exposure, which was presumably close to the resting state (for further details, see Section "Methods").

We adapted a spectral approach to estimate the timescales of resting-state neural activity from the ECoG dataset[11]. This method focuses on the Power Spectral Density (PSD) of the data, enabling reliable estimations of the time constant of neural activity from relatively short time series. In brief, we calculated the PSD of the activity data using Welch's method, followed by a Lorentz function fitting to determine the "knee frequency" and the corresponding decay time constant (see details in Section "Methods"). Previous studies anticipated an exponent of 2 for the Lorentz function[36], which has also been observed in our study, showing that the exponent clustered around 2 with minor variance in Fig. 1b.

By applying the spectral method, a prominent timescale gradient across 33 cortical areas was revealed. As illustrated in Fig. 1c, sensory areas including V1, V2, and AuA1 exhibited smaller time constants, while association areas, including A8aD, A10, and PG exhibited longer timescales. This trend was further substantiated by computing the average timescale for each category of areas, presenting a significant increase of timescales from the low-level sensory areas to the high-level association areas, as shown in Fig. 1d.

Intriguingly, our data analysis unveiled a striking consistency between the timescale hierarchy and the structural hierarchy assessed by the spine number of pyramidal neurons in each area[1,12]. As demonstrated in Fig. 1e, the timescale correlates strongly with the spine count across cortical areas. Furthermore, by analyzing the first 5 s of awake resting-state recordings[37], we observed a clear intrinsic timescale hierarchy across cortical areas closely matching the anesthetized state (Fig. S9a, b), with a strong correlation confirming consistency in the relative ordering of timescales (Fig. S9c).

Those findings propelled us to construct a multi-regional model of the marmoset neocortex that links the structural and dynamical property of the neocortex. With such a model, we were able to investigate how network structure shapes signal integration reflected by the neural time constant within each area and signal propagation across areas in the cerebral cortex – in particular, the role of the macroscopic gradient of spine count and the inter-areal connectivity.

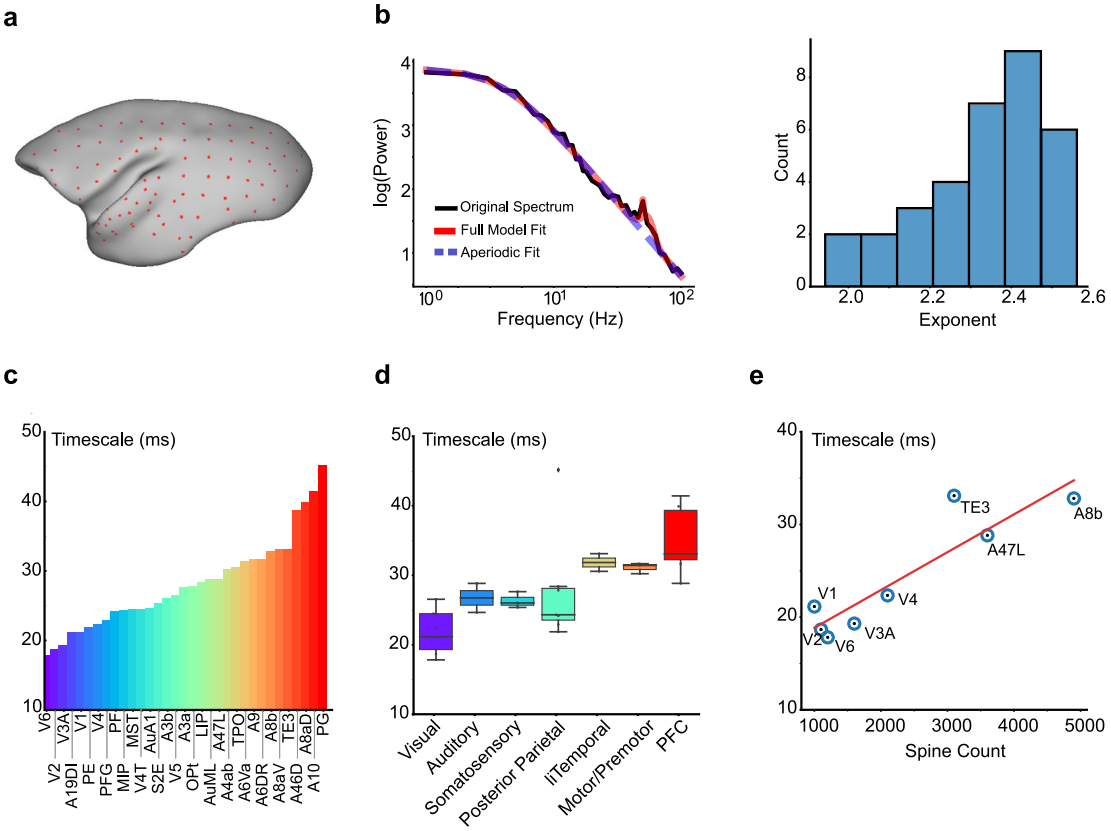

Fig. 1 | Experimental observation of timescale hierarchy in the marmoset neocortex. a The spatial distribution of electrode locations marked by red dots, adapted from electrode annotations in Nakae et al.[35] under a Creative Commons Attribution 4.0 International License (CC BY4.0). **b** Methodology for timescale measurement. Left panel: Exemplification of the Power Spectral Density (PSD) fitting process. Right panel: Distribution of the exponent values derived from the Lorentz function fit of the power spectrum. **c** Timescale distribution across the marmoset neocortex. Lower-level sensory areas such as V1, V2, and AuA1 exhibited shorter timescales, in contrast to higher-level areas like A8aD, A10, and PG that exhibited longer timescales. **d** Boxplot of timescale statistics for each areal category. Box plots show the median and IQR, with whiskers extending to the minimum and maximum values excluding outliers. Sample sizes (n, number of distinct brain areas per region) from left to right are $n = 9, 2, 3, 7, 2, 3$, and 7. **e** Positive correlation between timescale and spine count of pyramidal neurons for each area, revealing the structural-dynamical relationship (Pearson $r = 0.91$, $p = 1.91 \times 10^{-3}$). The timescales are fitted using the experiment data from an anesthetized marmoset[34].

A multi-regional model of the marmoset neocortex

We next developed a multi-regional model of the marmoset neocortex. The form of the model was adapted from Ref. 1 that described the macaque neocortex, considering the anatomical resemblance between the macaque and marmoset cortices. The model encapsulates 55 distinct sensory and association areas of the marmoset neocortex, including the 33 areas recorded in the previous experiment[34]. Each area in our model encompasses an excitatory and inhibitory neural population, both of which are locally interconnected with their activity described by the population firing rates. A detailed schematic of this multi-regional model is presented in Fig. 2a, b.

The network connectivity of the model was determined by the up-to-date anatomical measurement using retrograde tracing[25,26]. The magnitude of the directed connection between any two areas was derived from FLN determined through tracer injection experiments. The FLNs quantify the fraction of neurons projecting to a target area across all source areas, which can be viewed as a proxy of connectivity strength between two areas in our model. A heatmap representation of the FLN matrix is shown in Fig. 2c. The dynamical interactions within each area are described following a Wilson–Cowan type model (see further details in Section “Methods”).

In addition, the model accentuates the influence of the excitation gradient in scaling connection strengths between neural populations. Following prior macaque neocortex modeling[1], we integrated a composite gradient of excitation level across areas in the model, which mainly reflects the areal specific spine numbers of pyramidal neurons based on a previous anatomical study[26]. In our model, this composite gradient index has been additionally constrained to align with the experimentally measured timescales deduced from the ECoG data, as detailed in the preceding section. A detailed methodology for estimating the composite gradient is described in Section “Methods”. The composite gradient’s barplot is shown in Fig. 2d, alongside the average composite gradient for each category of cortical areas in Fig. 2e, revealing a statistically significant upward trend from visual areas to the prefrontal cortex. Furthermore, Fig. 2f illustrates the correlation between the composite gradient and the spine number of pyramidal neurons for all areas[26], demonstrating that the composite gradient index was predominantly determined by the spine number of pyramidal neurons, thus as a proxy of excitation level for neurons in each area.

While subcortical structures (e.g., thalamus, brainstem, basal ganglia, cerebellum) and peripheral sensory pathways (e.g., retina, cochlea, spinal cord) exert influences on cerebral cortical dynamics, the present model is restricted to cerebral cortical networks due to the absence of a marmoset-wide, high-resolution subcortical and peripheral connectome. It is worth noting, however, that this work focuses on timescales of spontaneous neural activity during the resting state, when there is no experimentally designed sensory stimulation to peripheral structures, and animals are not engaged in a particular task. As future anatomical data

https://doi.org/10.1038/s41467-025-66699-4

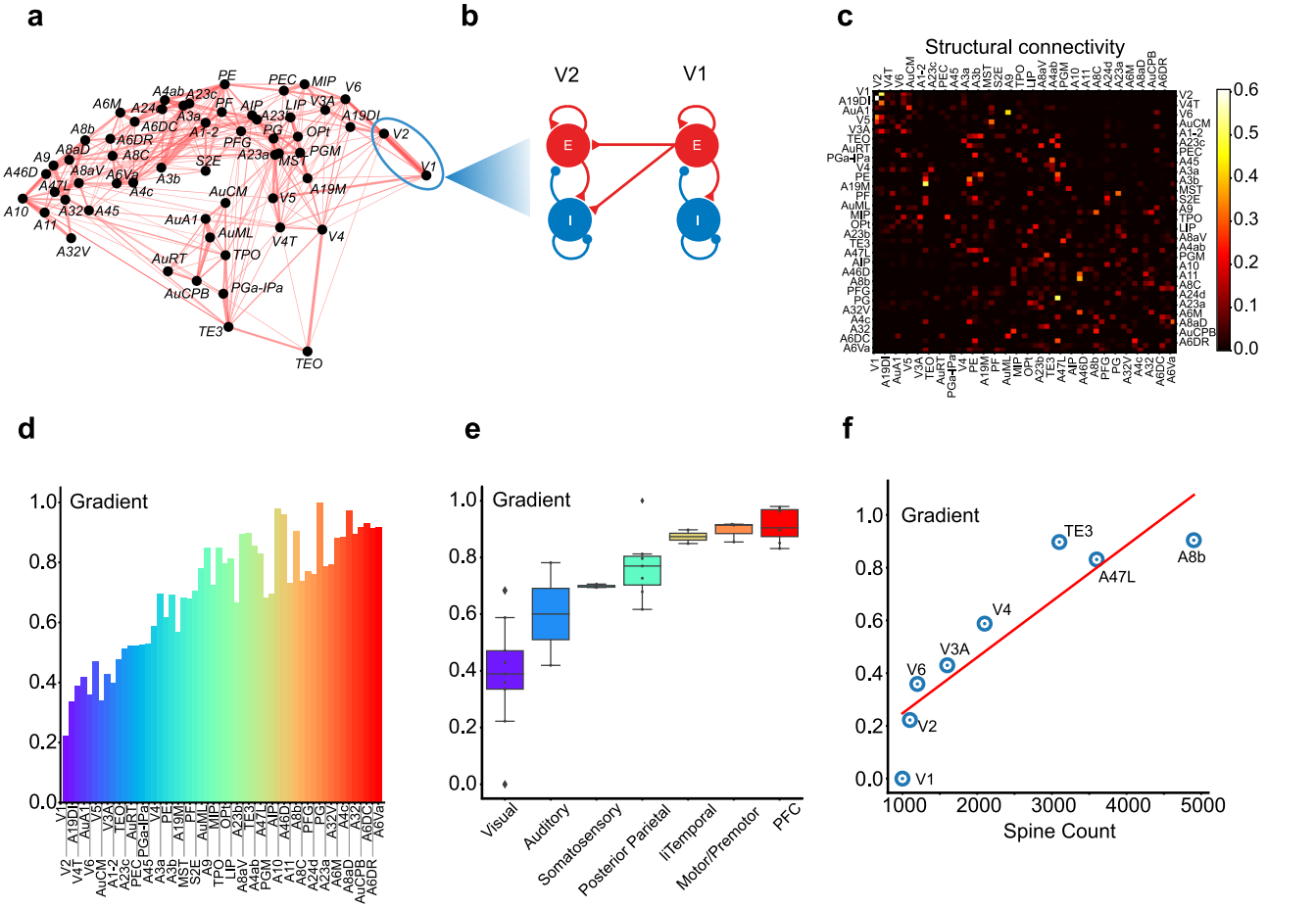

Fig. 2 | Properties of the multi-regional model of the marmoset neocortex. **a** Graph representation of the marmoset cortical areas, with line width representing connection strength (only the strongest 25% of connections are displayed). **b** Schematic depiction of the model area representing each cortical area, comprising excitatory and inhibitory neural populations with the directed interaction from Area V1 to Area V2 shown. **c** Matrix of connection strengths across all cortical areas. The directed connection magnitude between any two areas is based on the Fraction of Labeled Neurons (FLN) data derived from refs. 25,26. Only inter-areal (long-range) projections are shown for clarity. **d** Area-wise composite gradient of excitation in the model. **e** Boxplot of the composite gradient of excitation grouped by the category of areas, signifying a significant progression from visual areas to the prefrontal cortex. Box plots show the median and IQR, with whiskers extending to the minimum and maximum values excluding outliers. Sample sizes (n, number of distinct brain areas per region) from left to right are $n = 9, 2, 3, 7, 2, 3$, and 7. **f** Strong correlation between the model's composite gradient of excitation and the experimentally measured spine number of 8 areas (Pearson $r = 0.89$, $p = 2.6 \times 10^{-3}$). Layer-3 pyramidal-cell spine counts were taken from the cross-area compilation in Supplementary Table 4 of[26]; sampling details are given in the cited source articles.

allow the integration of subcortical and peripheral circuits, these additional components are expected to improve our model predictions of timescales and signal propagations, with the specific patterns likely influenced by interactions involving subcortical and peripheral structures.

Emergence of timescale hierarchy in the marmoset network model

We next investigated the capability of our model in replicating the experimentally observed timescales for each area in the marmoset neocortex. In simulating the model's resting state, we applied white-noise stimuli across all brain areas, to emulate the resting state scenario in experiment. The neural activities in various areas, illustrated in Fig. 3a, reveal that lower-level areas resonate at higher frequencies, akin to the input white noise. In contrast, higher-level areas exhibit smoother variations, reflecting their differing operational timescales. Further inspection of the auto-correlation function of activity within each area, as shown in Fig. 3b, demonstrates an evident exponential decay, though with significant variability in the decay time constants across areas, thus reinforcing the existence of different operational timescales in each area.

We then examined the timescale gradient more closely by estimating timescales from the PSD of the simulated neural activity, following the same approach used for the experimental data processing. As displayed in Fig. 3c, the timescale for each area forms a gradient ranging from 50 ms to 250 ms. This gradient rises from sensory to high-level areas, echoing the experimentally observed pattern. Next, we quantitatively compared the experimentally measured and model-predicted timescales area by area. Figure 3c shows a strong correlation between them, with a scaling factor around 5. This scaling is consistent with the findings in ref. 11 where the timescale of ECoG was compared with the timescale of neuronal firing activity. These outcomes suggest our model well captures the experimental observations, thus validating the model's effectiveness. Moreover, the timescale gradient and its close consistency with experimental data remain robust even when biologically realistic axonal conduction delays are incorporated into the model (Fig. S8). Finally, Fig. 3d demonstrates that the consistency between the time constant and the spine number across areas is also preserved in our model.

Furthermore, we substantiated the property of timescale gradient by examining the eigenmodes in the modeled system. For each eigenmode (a column of the matrix in Fig. 3e), each entry implies that

https://doi.org/10.1038/s41467-025-66699-4

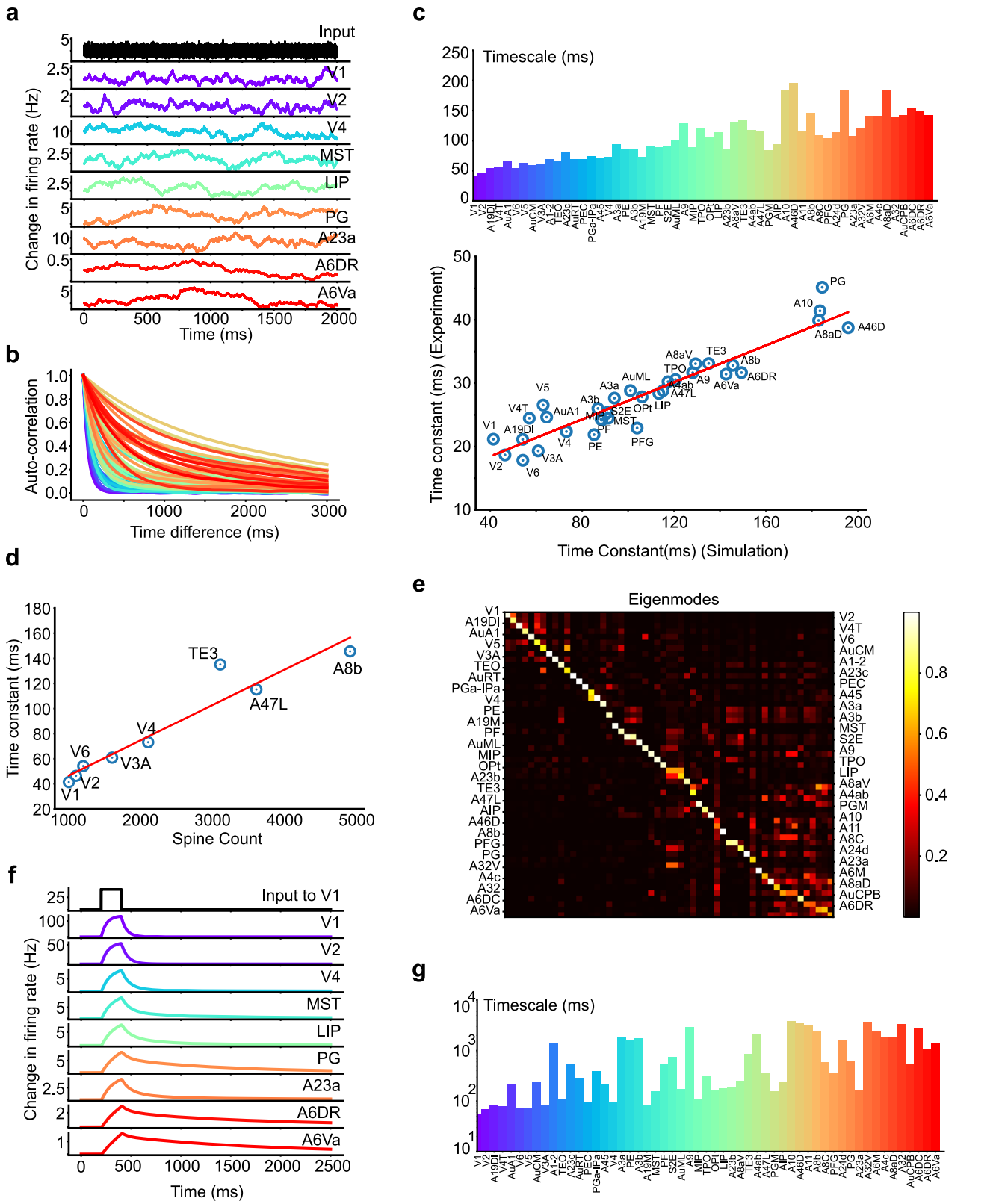

Fig. 3 | Investigation of timescale gradient and localization in the model. **a** Simulated resting state activity, with white-noise input to all brain areas. Lower-level areas resonate at higher frequencies, whereas higher-level areas show more gradual fluctuations. **b** The autocorrelation function of each area's activity in the resting state. **c** Top panel: The timescale derived from the Power Spectral Density (PSD) of simulated resting state activity, forming a gradient spanning from 50 ms to 250 ms. Bottom panel: Strong correlation of timescale between model and experiment (Pearson $r = 0.94$, $p = 6.57 \times 10^{-16}$). **d** Significant correlation between the simulated timescale and spine number (Pearson $r = 0.95$, $p = 2.18 \times 10^{-4}$). **e** Visualization of the dynamical system eigenmodes. The timescale localization for each area is portrayed by the sparseness of the eigenmodes. **f** The activity of selected areas following a stimulus to V1 in the model. Decay time constant increases along the signal propagation pathway. **g** The observed timescale gradient following a stimulus to V1, as extracted by fitting to the exponential function.

the neuronal activity in the corresponding area will possess a timescale determined by the eigenvalue of that eigenmode. Thus, a sparse eigenmode indicates that only a few areas exhibit a particular timescale determined by the corresponding eigenvalue, supporting the concept of "timescale localization". Figure 3e illustrates the phenomenon of timescale localization as indicated by the eigenmode matrix's resemblance to a block diagonal matrix. Such an observation is instrumental as it indicates the capacity for lower-level sensory areas to respond quickly to incoming stimuli and discard older inputs. Conversely, higher-level planning and decision-making areas retain information over extended periods, aiding in integrative processes such as working memory.

We further studied the timescale gradient in the presence of stimulus in the model. By recording the post-stimulus response for all areas after activating the V1 area, Fig. 3f demonstrates that activity in high-level areas (PG, A6DR, A6VA, etc.) persisted longer than in lower-level visual areas (V1, V2, V4, etc.), reflecting a functional facet of the timescale gradient. A further quantitative investigation of this gradient by an exponential fit to the activity data (details in Section "Methods") was depicted in Fig. 3g. Intriguingly, the auditory areas, typically considered lower-level but not directly involved in visual stimulus transmission, showed a longer timescale. This observation can potentially be attributed to the absence of direct connections between visual and auditory cortices. Hence, when the visual cortex is stimulated, the auditory cortex may be indirectly activated through high-level cortical areas operating over longer timescales. As a result, the auditory cortex, receiving inputs over extended periods, also exhibits these longer timescales, as depicted in Fig. 3g.

Figure S1a presents a direct comparison of timescales during rest and post-V1 stimulus, revealing a marked similarity between the two timescales derived under different brain states. Notably, higher-level areas exhibit longer timescales than lower-level ones, with exceptions like the auditory cortex discussed previously. We attribute these differences to the external stimuli on specific brain areas. Further mathematical analysis and numerical simulations (Supporting Information and Fig. S1b–e) clarify that the post-stimulus timescale of area activity is influenced by the system eigenmodes' intrinsic timescales and the stimulus-induced multi-regional activity pattern. Importantly, the external stimulus does not alter the network's intrinsic timescale or eigenmode pattern but modifies the contribution of each intrinsic timescale (and the corresponding eigenmode) to the activity of cortical regions.

Essential conditions on timescale localization

We next studied the mechanism underlying the property of timescale localization. A previous theoretical study of the macaque neocortex[31] has proposed essential conditions for achieving timescale localization: the macroscopic gradient of excitation across areas and the balance of excitatory and inhibitory inputs received by each area. The macroscopic gradient refers to the gradual varying excitation strength across different cortical areas indicated by spine number of pyramidal neurons in each area, while "E-I balance" alludes to the delicate current cancellation between global long-range excitatory inputs and local inhibitory synaptic inputs to the excitatory neural population in each area.

To examine these two conditions in the marmoset cortical network, we first introduced two metrics for eigenmodes – the Inverse Participation Ratio (IPR) and the θ index to quantify the timescale localization and its spatial localization, respectively (see both definitions in Section "Methods", θ was initially proposed in Luis Carlos Garcia and Xiao-Jing Wang, see[38]). A higher IPR value (closer to 1) indicates a particular timescale localized in fewer number of areas, and a higher θ index (closer to 1) describes a timescale localized in physically more proximal areas. For the model detailed previously, the scatterplot of IPR and θ for each eigenmode of the model system is shown in Fig. 4a, while the timescales of each eigenmode is indicated by the color code. Examples of eigenmodes with different IPR and θ are presented in Fig. S2. As shown in Fig. 4a (left panel), both high IPR and θ are observed for most eigenmodes, demonstrating that the timescale localization is present in the model, and each timescale is spatially localized in physically neighboring areas.

Subsequently, we examined the conditions for timescale localization in the marmoset neocortex. By removing the macroscopic composite gradients (setting the gradients h_i to zero for all areas in the model), we observed a marked degradation of timescale localization and spatial localization, as evidenced by significantly smaller IPR and θ (Fig. 4a, right panel). Notably, the range of eigenmode timescales becomes narrower and more concentrated (predominantly around 50 ms), underscoring the influence of the composite excitation gradient in extending timescales. Further exploration involved adjusting the gradient's slope (multiplying the gradient h_i with a factor γ for all areas in the model) and observing the resulting changes of timescale localization. We found a progressive increase in IPR from 0.1 to 0.65 and θ from 0.65 to 0.95 as the gradient slope γ varies from 0 to 1 (Fig. 4b), supporting the pivotal role of the macroscopic gradient of excitation in timescale localization and its spatial distribution. The effect of the gradient of excitation becomes even more apparent when comparing the eigenmodes of the network with and without the gradient. Figure 4c, d showcases the fastest eigenmode for both scenarios (edged in black in Fig. 4a). While both eigenmodes predominantly involve low-level visual areas with V1 activity dominating the eigenmode, the eigenmode in the control condition is markedly sparser, highlighting the dominant role of V1 activity. This comparison demonstrates the composite gradient's contribution to timescale localization, even within the low-level sensory cortex.

In a parallel model simulation, we disrupted the E-I balance in our model by increasing the strength of local connections from inhibitory to excitatory neurons (ω_{EI}). This modification leads to the imbalance between the global long-range excitatory inputs and the local inhibitory synaptic inputs. Consequently, it resulted in smaller IPR and θ that reflect poor timescale localization and spatial localization (Fig. 5a), similar to the case of gradient removal. With the E-I balance disturbed, the eigenmode characterized by the shortest timescale no longer involved the primary visual cortex (Fig. 5b). This shift underscores the critical function of E-I balance, not merely as an essential condition for timescale localization but also as a determinant in the gradient of timescales from low-level sensory to high-level brain areas.

In our continued exploration, we probed the influence of long-range connections on timescale localization. When connectivity strengths (FLNs) were randomly shuffled, as illustrated in Fig. 5c, the cortical network preserved high IPR values similar to the control condition (Fig. S3), indicating robust timescale localization. However, θ index reduced significantly, suggesting a decrease in spatial localization of timescales. This effect is also evident using the example of the slowest eigenmode in both the shuffled FLN network and the control condition, as illustrated in Fig. 5d and Supplementary Fig. S2e, respectively. Notably, while both eigenmodes encompass a variety of brain regions, including notably the prefrontal cortices, the eigenmode under the shuffled FLN condition exhibits a broader distribution, extending to primary visual and auditory cortices. In contrast, the eigenmode in the control condition demonstrates greater spatial localization, predominantly engaging high-level brain areas.

Besides the reduced spatial localization, the range of timescales was also narrowed compared to the control condition. These observations were further substantiated by the results from 1000 repetitions of FLN shuffling. Disrupting these long-range connections led to a noticeable contraction in the timescale range and diminished spatial localization, as evidenced in Fig. 5e, f. These results underscored the significant role of long-range connections in timescale localization, i.e., nearby areas process signals with similar timescales reflected by high θ value, while areas with some distance possess a variety of timescales

https://doi.org/10.1038/s41467-025-66699-4

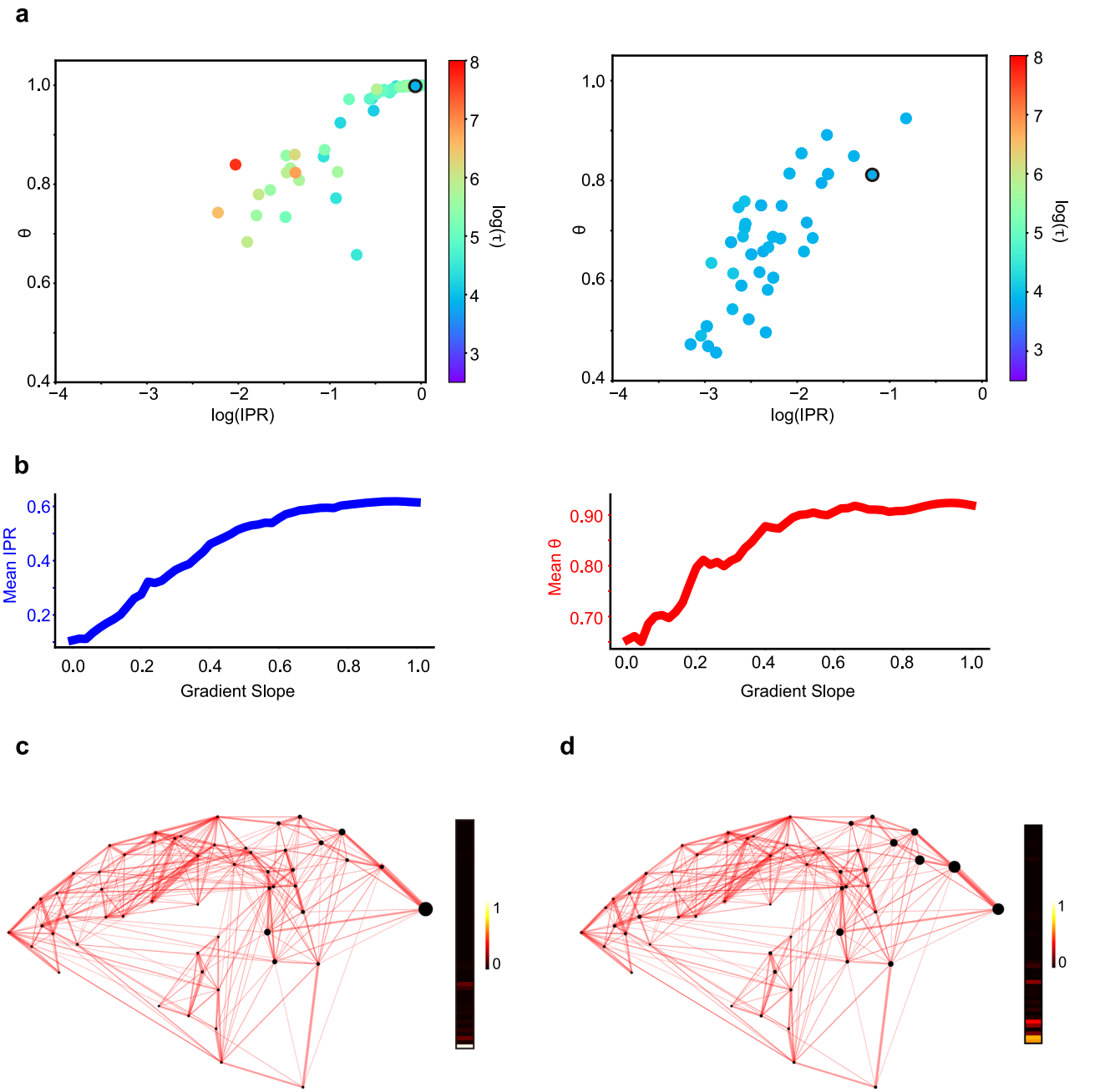

Fig. 4 | Effect of macroscopic gradient of excitation on timescale localization. **a** Scatterplot of Inverse Participation Ratio (IPR) and θ for each eigenmode of the modeled dynamic system. Left panel: plot under the control condition. Right panel: plot under the condition that the composite gradient of excitation is absent. The color-coded timescale was after taken the logarithm using the natural base e. **b** Change of IPR (left panel) and θ (right panel) as the gradient slope increases. **c** Visualization of a representative eigenmode (the fastest eigenmode) in the control condition, with values of the eigenmode plotted aside. The size of each black dot codes the magnitude of the corresponding element in an eigenmode. **d** Similar to (**c**), under the condition that the composite gradient of excitation is absent. The eigenmodes correspond to the black-circled dot in (**a**).

enabling hierarchical signal processing. It suggests that the organization of the inter-areal connections is not random but is rather essential for brain functionalities.

Impact of near-critical state on structural and functional connectivity

As the macroscopic gradient of excitation largely influences timescales across areas, it is expected to influence the functional connectivity (FC) that relies on the temporally co-activation of pairwise areas. On the other hand, the macroscopic gradient also adjusts the effect of structural connectivity (SC) as the FLN will be scaled by the composite gradient as a proxy of the spine number of neurons in each area. Therefore, in this section, we direct our attention to how the macroscopic composite gradient shapes the correlation between SC and FC. We initiated this investigation by removing the gradient from our model and computing the resultant FC. Under these conditions, the simulated FC from our model significantly aligns with the SC. This increased correlation, contrasted with the dissimilar case in the presence of gradient of excitation (visualized in Fig. 6a), suggests that the composite gradient can contribute to high-order connections within FC. These findings underscore that the composite gradient, as a fundamental structural attribute, can significantly shape the functional

https://doi.org/10.1038/s41467-025-66699-4

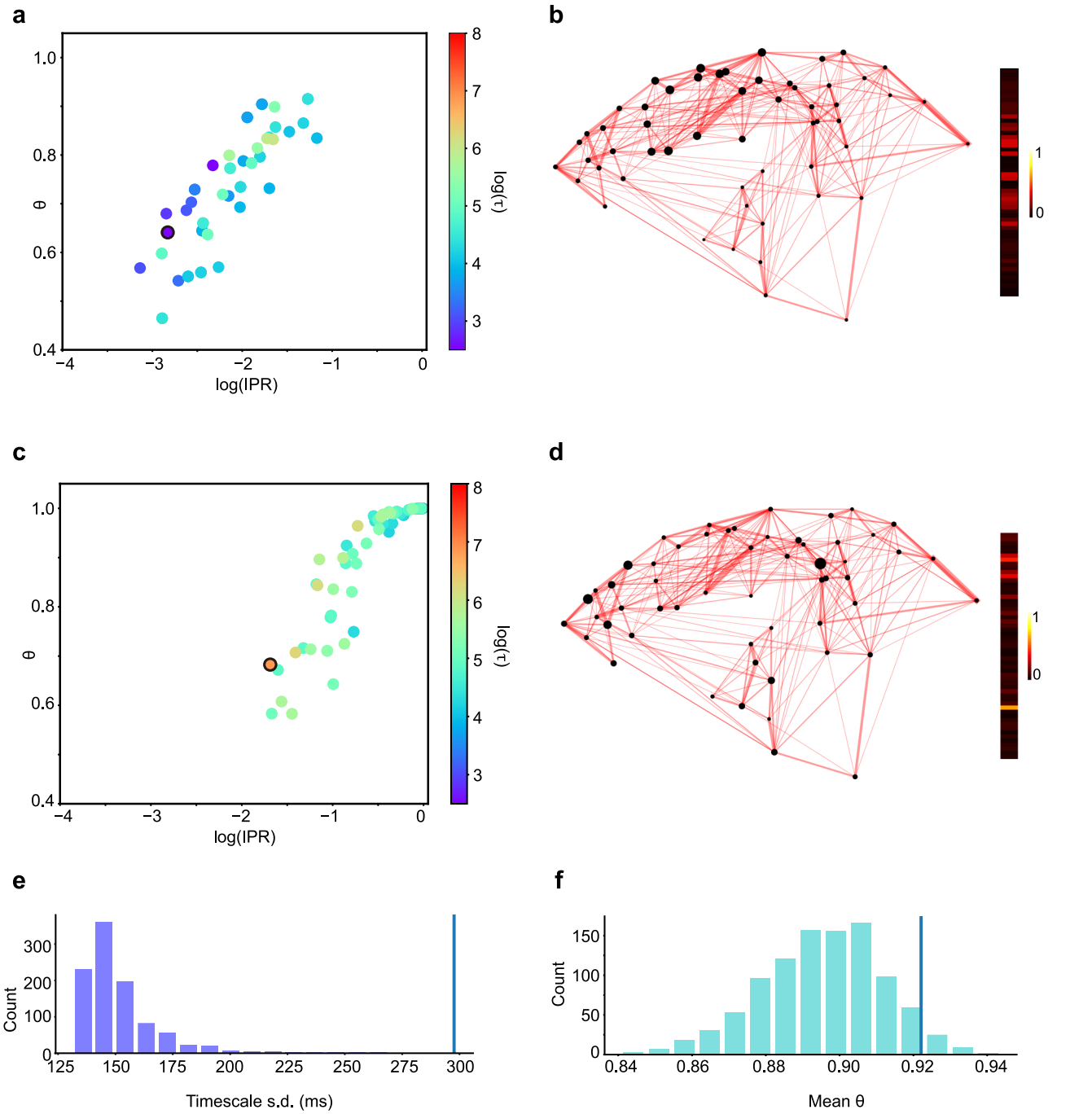

Fig. 5 | Essential conditions of timescale localization. a Scatterplot of Inverse Participation Ratio (IPR) and θ for each eigenmode of the modeled dynamical system similar to Fig. 4a, under the condition that the E-I balance is disrupted by increasing w_{EI} by 10%. **b** Visualization of the fastest eigenmode (black-circled dot in (**a**)), alongside the values of eigenmode, under the condition that the E-I balance is disrupted by increasing w_{EI} by 10%. **c** Similar to (**a**), but the FLN matrix is shuffled. **d** Similar to (**b**) but showing the slowest eigenmode (black-circled dot in (**c**)) with the shuffled FLN matrix. **e** Impact of shuffled FLNs on timescale range. The histogram of the timescale range quantified by the standard deviation of timescales after randomly shuffling FLNs. **f** Impact of shuffled FLNs on spatial localization. The histogram of the degree of spatial localization quantified by the θ metric with randomly shuffled FLN. Both distributions (**e**, **f**) are significantly smaller than the values observed in the control condition, as indicated by the vertical lines.

interplay between different brain areas. This phenomenon was consistent with that observed in the macaque neocortex model[1], yet the mechanism remains to be elucidated.

Here we further developed a mathematical analysis to identify a quantitative relationship between FC and SC and investigated their relationship when the macroscopic gradient of excitation exists, following the analysis in ref. 39. As shown in Fig. 4a, the composite gradient gives rise to a wide range of timescale pool, in which the slowest timescale can be as long as hundreds of milliseconds or longer. The very slow timescale attributes to an eigenvalue close to zero, which indicates that the cortical network operates close to the critical state (the edge of stability). Building upon these facts, we mathematically analyzed the effects of criticality on the SC and FC relation (see Section Supporting Information), proving that the dissimilarity between FC and SC substantially increases when the network state approaches criticality.

https://doi.org/10.1038/s41467-025-66699-4

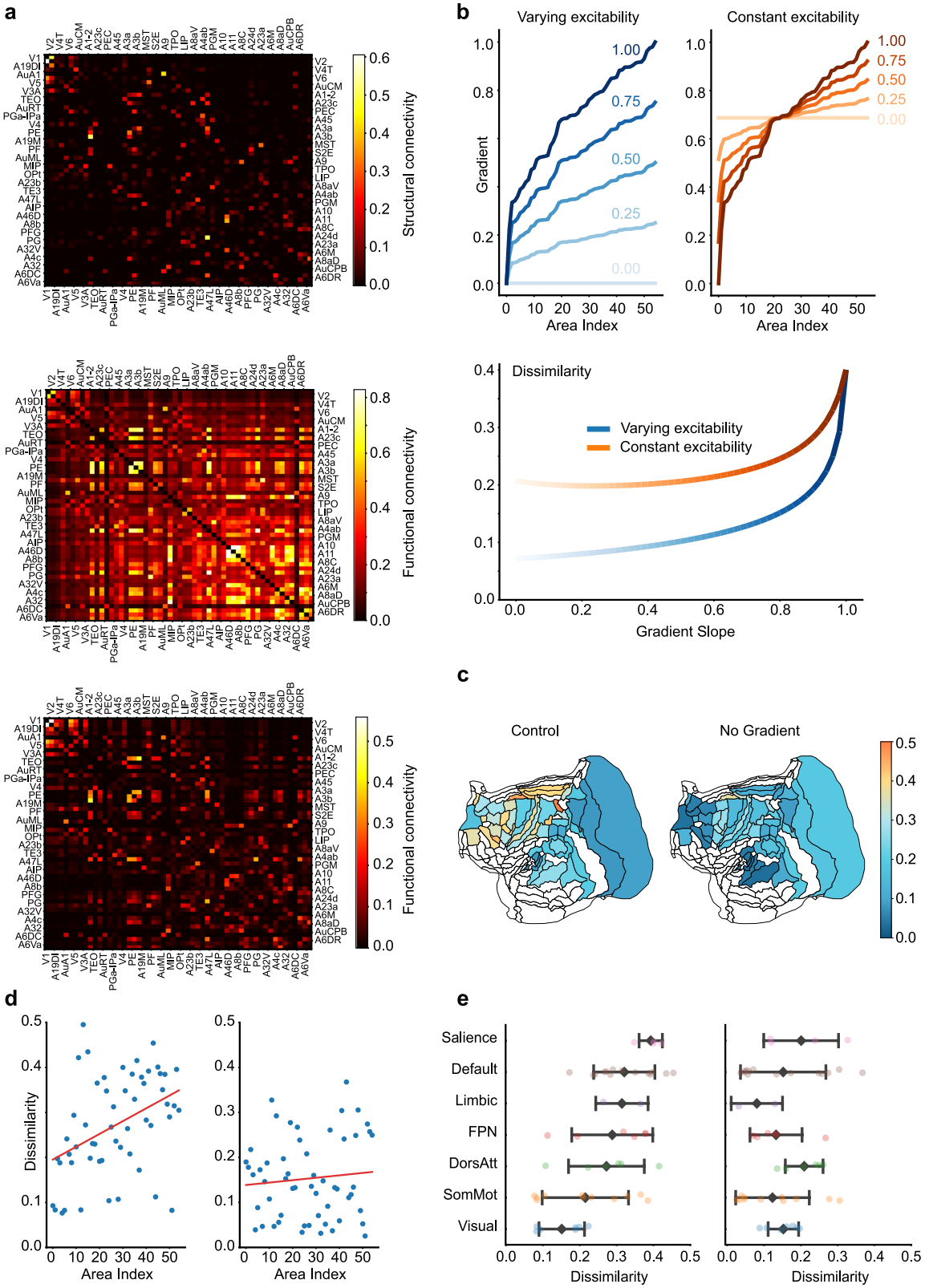

We next scrutinized the role of the composite gradient on network criticality by adjusting its slope, akin to the model simulations conducted when investigating timescale localization. Specifically, we manipulated the slope of the gradients in two distinct ways: by either maintaining the average gradient value constant or allowing it to vary. Figure 6b (top panel) displays examples of these gradient adjustments for various gradient slope by each method. As depicted in Fig. 6b (bottom panel), the dissimilarity between FC and SC intensifies with steeper gradient slope, confirming our hypothesis that composite gradients can contribute to the system's criticality and, subsequently, the dissimilarity between FC and SC. We further explored the gradient's function by maintaining the average excitability of all areas as a constant. Remarkably, even when the average excitability remains constant at the whole-cortex level, composite gradients can enhance

Fig. 6 | Impact of critical state on structural and functional connectivities. **a** Depiction of structural connectivity (SC) and functional connectivity (FC) under various scenarios. Top panel: Plot representing structural connectivity (SC) as per the FLN matrix. Middle Panel: Visualization of FC, measured by the correlation coefficient between resting-state neural activity from different areas, with the presence of composite gradient. Bottom Panel: Visualization of FC in the absence of composite gradient. **b** Dissimilarity between FC and SC as a function of gradient slope. Top panel: Illustration of two distinct approaches to modifying the gradient slope, depicted through a color gradient from dark to light, indicating a change in slope from 1 to 0. Left, the adjustment of gradient slope with varying excitability. Right, the adjustment of gradient slope with constant average excitability. Bottom panel: The dissimilarity increases with the slope of gradient, with or without average excitability held constant. Here the dissimilarity is quantified as $1 - |\rho|$, where ρ is the Pearson correlation between FC and SC. **c** Heatmap of FC-SC dissimilarity across different brain areas, shown in marmoset brain parcellation. Left: FC-SC dissimilarity produced by the control model with composite gradient. Right: the model result with composite gradient removed. **d** Left, correlation between the FC-SC dissimilarity for each brain area ranked by its composite gradient of excitation in an ascending order (Pearson $r = 0.41$, $p = 2.12 \times 10^{-3}$). Right, absence of this correlation when the gradient is removed ($r = 0.09$, $p = 0.491$). **e** FC-SC dissimilarity across seven functional subnetworks of the marmoset brain. Left: the control model result. Right: The model result with gradient removed. Each dot represents the FC-SC dissimilarity of an individual brain area. Larger overlaid points show the mean for each subnetwork, and error bars denote ±1 standard deviation around the mean. Sample sizes (n, number of distinct brain areas per subnetwork) from bottom to up are $n = 7$, 11, 6, 6, 2, 14, and 4.

local excitability and increase the dissimilarity between FC and SC (Fig. 6b, bottom panel).

Next, we turned to analyze the impact of the composite gradient on individual cortical areas. Through mathematical analysis, we proved that the correlation between FC and SC is significantly lower in association areas compared to early sensory areas (see Section Supporting Information), which has also been reported experimentally in a monkey study[40]. In the model simulation, we computed the dissimilarity between FC and SC for each cortical area and visualized these differences in a marmoset brain parcellation (Fig. 6c, left panel). The simulation results confirmed that dissimilarity is substantially higher in association areas than in early sensory areas. This trend is not evident when the composite gradient is absent (Fig. 6c, right panel).

To further quantify this observation, we identified a positive and significant correlation between FC-SC dissimilarity and the rank of each area's composite gradient (Fig. 6d, left panel). In contrast, this correlation disappears when the gradient slope is zero (Fig. 6d, right panel), indicating that this effect is not solely due to the heterogeneity of inter-areal connectivity. We further validated this by categorizing marmoset brain areas into seven subnetworks, comparable to those reported in humans[41] and macaques[42]. As shown in Fig. 6e, FC-SC dissimilarity is relatively small for lower-level visual and somatic motor subnetworks, but becomes more significant in higher-level association subnetworks. These findings are consistent with previous findings on human cortex[42,43] and are absent when the gradient slope is removed (Fig. 6e, right panel). This gradient-facilitated feature underscores the importance of higher-level areas in establishing wide-ranging functional connections, thereby supporting the execution of complex cognitive functions. These insights reaffirm the crucial role that gradients play in brain functionality.

The critical state of the model not only depends on the composite gradient of excitation across areas but also on the inter-areal connection among areas. To study the effect of inter-areal connection on the FC-SC relation, we first removed the gradient from our model and studied the impact of increasing the inter-areal coupling strength of excitatory inputs. As the coupling strength escalates, the network state gets closer to criticality, resulting in an increased deviation between FC and SC. This trend, as depicted in Fig. S4, is also consistent with our mathematical analysis (see Section Supporting Information).

Signal propagation in the near-critical state

In this section, we first investigated how the signal propagates across areas within our model, drawing parallels with observations from a previous optogenetics experiment[37]. In the experiment[37], an input was given to the marmoset A4ab area via an LED optogenetic stimulation, and ECoG data were recorded from 64 electrodes broadly distributed on the marmoset neocortex. We replicated this experimental stimulus protocol within our model and analyzed the peak responses, defined as the highest level of neural activity observed in each cortical area post-stimulus. As shown in Figs. 7a and S6, our model well aligns with the experimental measurements for the majority of cases without additional parameter tuning, affirming the physiological relevance of our model's responses. Similarly, this strong agreement with experiments was conserved after incorporating biologically realistic axonal conduction delays into our model (Fig. S8).

We then examined the necessary conditions for signal propagation within the model starting from a pulse stimulus applied to sensory cortices, such as the primary visual cortex (V1), a central source of visual input. Responses from critical cortical areas were depicted in Fig. 7b, showing steady signal propagation from the visual cortex to high-level areas like the prefrontal cortex.

We next investigated the role of inter-areal connectivity for signal propagation. The connectivity can be classified into feedforward and feedback connections based on anatomy[25,26]. As intuitively expected, eliminating feedforward connections significantly hampers signal propagation from sensory areas (data not shown). We then shifted our focus to the role of feedback loops. These loops consist of connections from high-level areas to low-level areas identified by a smaller fraction of neurons in a projection originating from the supragranular layers of the source area (SLN < 0.5)[25,26]. As demonstrated in Fig. 7c (orange line), the deletion of all feedback loops within the FLN precipitates a generalized decrease in peak responses across all areas, with low-level areas bearing the brunt of this impact. Subsequent analyzes investigated the influence of the composite gradient of excitation on signal propagation. As shown in Fig. 7c (green line), the absence of the composite gradient led to a significant reduction in neural responses, particularly in higher-order areas. To explore this effect further, we systematically varied the gradient slope and examined the resulting changes in signal propagation, using peak responses from the PG area as a metric. As illustrated in Fig. 8a, increasing the gradient slope enhanced signal strength, highlighting the critical role of gradients in facilitating signal propagation.

The contrast in signal propagation effects between the removal of excitation gradient and feedback connections is notable. The composite gradient of the excitation enables the high-level brain areas to receive stronger recurrent excitatory input, substantially amplifying long-range inputs from lower-level areas. In contrast, feedback connections enable indirect interactions between different lower-level areas via top-down projections from higher-level areas, significantly benefiting signal propagation, especially between areas lacking direct connections.

Building on the central role of both feedback loops and composite gradients in driving the system toward a critical state, our study delved deeper into the interplay between system criticality and the coexistence of signal propagation and integration. We examined the effects of altering global excitatory-excitatory (E-E) connectivity (μ_{EE}), while maintaining a constant global excitatory-inhibitory (E-I) strength (μ_{IE}), on the signal propagation and integration. Our findings, presented in Figs. 8b, c, and S7, elucidate several key insights. Firstly, the criticality of the system, implemented by the balance between μ_{EE} and μ_{IE}, emerges as an important determinant of neuronal activities. An imbalance, particularly at lower μ_{EE} levels, markedly impairs both

https://doi.org/10.1038/s41467-025-66699-4

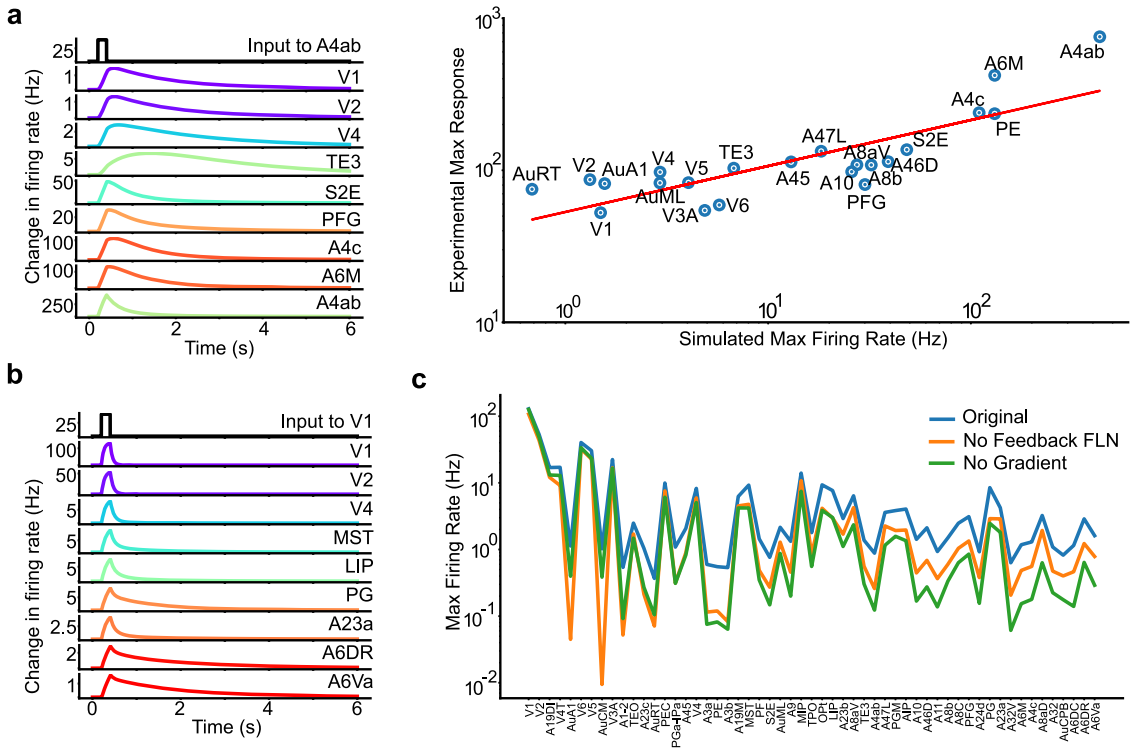

Fig. 7 | Signal propagation in the model. a Comparison of the model's response post-stimulation to A4ab with corresponding optogenetics data. Left panel: Activity of representative areas following A4ab stimulation. Right panel: Comparison of the model's peak response with optogenetics experimental data, demonstrating high model-experimental data consistency (Pearson $r = 0.82$, $p = 3.21 \times 10^{-6}$). **b** Activity of representative areas following V1 stimulation. **c** Comparison of the model's response in the control condition with the scenario when the feedback loops within FLN are eliminated and the scenarios where the composite gradients are removed.

signal propagation and integration. Furthermore, we observed a trade-off regime (grey areas in Figs. 8b, c, and S7) when μ_{EE} approaches the critical threshold, highlighting the intricate balance between signal propagation and integration. Approaching this threshold enhances signal propagation and enlarges the range of timescales, albeit at the expense of reduced timescale localization. Additionally, our results demonstrate that under conditions of strong global interaction strength (solid lines in Fig. 8b, c, and S7), both signal propagation and integration sustain high baseline values within the critical zone. This suggests that strong global connectivity, nudging the system toward criticality, is crucial in facilitating the co-existence of global signal propagation and localized integration.

Discussion

We reported empirical evidence for a hierarchy of time constants in the marmoset cerebral cortex and developed a connectome-based model of the marmoset neocortex. The key findings are threefold. First, a macroscopic gradient of synaptic excitation across areas, a detailed balance between excitatory and inhibitory populations, and the arrangement of long-range connections are instrumental in achieving timescale localization. Second, the state of the network operates close to criticality, an observable manifestation of which is the substantial dissimilarity between structural and functional connectivities, thus shaping the functional interaction between diverse areas of the neocortex. Third, our model accounts for experimental observations of signal propagation dynamics, underscoring the importance of the criticality facilitated by the feedback loops and the macroscopic gradients.

Criticality, or the edge of stability, is a state that can be signified by the system's largest eigenvalue approaching zero. In the cortical network, it unveils itself as a powerful influencer of cortical functionality. This unique state naturally is closely linked to an enlargement of timescales, enabling signal integration with longer timescales than characteristic neuronal membrane timescales (hundreds of milliseconds versus tens of milliseconds). Moreover, criticality, achieved not solely through the balance of local excitatory and inhibitory inputs but also through broader network dynamics, facilitates extensive communication between local areas and the global neural network. This, in turn, amplifies signal propagation, affirming the vital role of criticality in streamlining neural communication.

Converging evidence across multiple species and brain regions indicates that cortical dynamics operate near a critical point, yet remain slightly subcritical[44–46]. This slight subcriticality is exemplified by a consistent branching ratio of ~0.98 observed in vivo[46] and truncated neuronal avalanche size distributions in awake cortex[44,45]. Notably, the precise operating point can be modulated by brain states: focused attention shifts cortical activity further into the subcritical state from the near-critical state during resting[47], while changes in arousal or anesthesia can also influence the distance from criticality[48,49]. Operating just below criticality is hypothesized to confer several key functional advantages–ensuring stability against runaway excitation, preserving long-range correlations and large repertoires of activity patterns, enabling efficient information processing across a critical-like broad dynamic range, and allowing flexible tuning of network sensitivity[45,50]. Theoretically, the cortex's hierarchical modular architecture could yield an extended critical-like regime on the subcritical side (a Griffiths phase) that provides these functional benefits without fine-tuning[50]. Consistent with this "subcriticality" framework, our modeling results for the marmoset cortical demonstrate that a near-critical (slightly subcritical) state supports robust but controlled global signal propagation and naturally extended intrinsic timescales, highlighting how slight subcriticality effectively balances integration and stability while avoiding the fragility associated with exact criticality.

Our simulations and analysis further spotlighted the substantial impact of operating near criticality on the dissimilarity between

https://doi.org/10.1038/s41467-025-66699-4

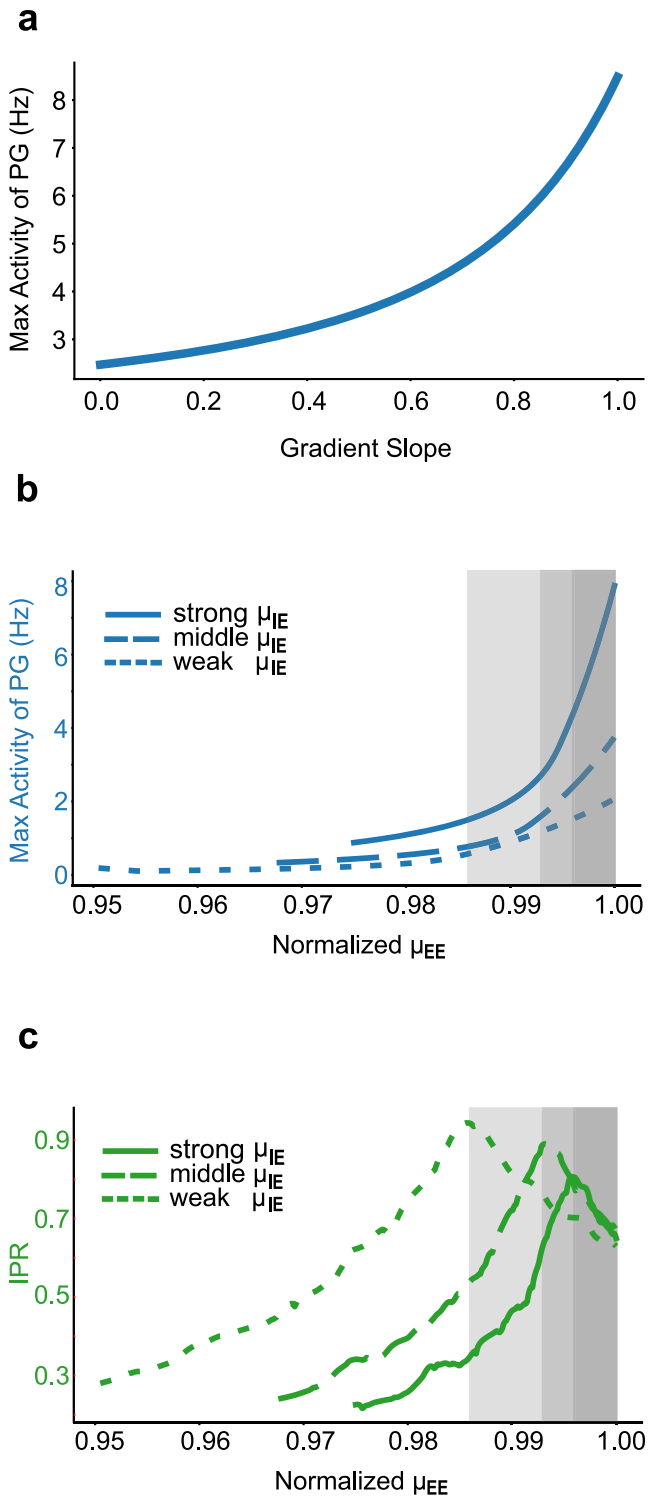

Fig. 8 | Signal Propagation and the critical state. a Illustration of a typical area (PG)'s response as a function of the slope of the composite gradient of excitability. **b**, **c** Impact of global excitatory connectivity (μ_{EE}) on signal propagation and integration, where μ_{EE} is normalized to its critical value -- the maximum at which the system retains stability. Line-types indicate different μ_{IE} values: 49.81, 37.36, 24.91 pA/Hz for strong (solid line), middle (dash line), weak (dot line) μ_{IE}, respectively. Gray shaded area: the parameter region where exists the trade-off between signal propagation and integration. **b** Effect of μ_{EE} on signal propagation, quantified by the maximum activity in area PG's response. **c** Effect of μ_{EE} on signal integration, quantified by Inverse Participation Ratio (IPR).

Functional Connectivity (FC) and Structural Connectivity (SC). As criticality escalates, the disparity between FC and SC widens. This divergence permits the routing and broadcasting of information even in the absence of direct connections, promoting broad-range neural communication. Several pieces of evidence support the view that criticality contributes to this divergence in cerebral cortex. For instance, a prior model-based study showed that an enhanced criticality in the model could generate an FC more similar to experimentally measured FC[39].

Furthermore, recent studies on the human cortex have shown that the strength of structural-functional coupling (SFC) is not uniform across the cortex, but tending to be stronger in primary and unimodal sensory regions while progressively weakening in higher-order association areas[42,43]. In line with these findings, our results demonstrate that applying a macroscopic gradient of excitation selectively modulates local criticality, enhancing signal integration and directing information flow in high-level cortices. As a result, functional patterns in these higher-order areas deviate more strongly from their underlying structural connectivity compared to lower-level areas (Fig. 6c), a divergence that may be crucial for supporting complex cognitive operations. Indeed, abolishing the gradient slope eliminates this spatially selective effect (Fig. 6d), suggesting that it is not solely due to the heterogeneity of inter-areal connectivity. We further confirm that the decrease in SFC with increasing cognitive representational hierarchy remains evident when marmoset brain areas are categorized into seven subnetworks: SFC is strong in lower-level visual and somatic motor subnetworks but weakens in higher-level association subnetworks (Fig. 6e). By tuning criticality through these macroscopic gradients, the brain may expand its range of potential activity states, thereby facilitating higher-order cognition.

Several elements of this study merit attention when compared with analogous previous modeling works on the macaque neocortex[1,33]. Based on a similar modeling framework of cerebral cortex, which includes (i) representing each brain area by both excitatory and inhibitory group neurons; (ii) connectivity between areas dictated by experimentally measured connectomes; and (iii) a macroscopic area-wise composite gradient scaling the strength of excitatory projections, our model reproduces several phenomena observed in earlier studies–timescale localization, signal propagation, and the dissimilarity between FC and SC- despite modeling a different species, the marmoset. This conservation across species emphasizes the robustness of the model framework as a sturdy base for future research probing the relationship between structure and function at a whole-brain level, including the interplay between cortical dynamics and subcortical or peripheral neural systems.

Nevertheless, important distinctions from prior work are worth noting. Although both our study and earlier work constructed models with structures and parameters bound by experimental constraints, our study further corroborates the model's responses with comparable experimental data across various scenarios, which allows us to compare the model and the experimental data area-by-area. We showed that the timescales for different areas predicted by the model and those measured in experiment under resting state (Fig. 3c), and the after-stimulus response (Figs. 7 and S6) well agree with each other. The strong concordance with experimental data not only affirms the model's validity but also accentuates its potential to probe intricate interactions within the cortical structural and functional dynamics.

Moreover, our model concurrently captures timescale localization[1] and signal propagation[33] with a single parameter set, which was not achieved in previous works. While Chaudhuri et al.[1] revealed that the presence of a gradient can facilitate timescale localization, it significantly dampened signal propagation. Conversely, Joglekar et al.[33] presented a model with satisfactory signal propagation

but impaired timescale localization. Our model not only captures both phenomena within the same parameter regime but also exhibits similar qualitative behaviors to both models. This includes the gradient dependency for timescale localization, the necessity to maintain a balance between excitatory and inhibitory inputs, and the requirement of feedback loops for signal propagation. Understanding why our model could embody both features within a single parameter regime demands further mathematical analysis of this multi-regional model with gradients of excitation.

Our analysis also underscores a phenomenon wherein variations in model parameters yield diverse effects on timescale localization, signal propagation, and system criticality. For instance, increasing the gradient slope concurrently enhances timescale localization and signal propagation, nudges the system towards criticality, and amplifies the dissimilarity between FC and SC. Conversely, increasing the global coupling strength of excitatory neurons (μ_{EE}) produces somewhat opposing effects. Although it boosts signal propagation and steers the system closer to criticality, thus increasing the disparity between FC and SC (Fig. S4), it also undermines timescale localization. This reduction in timescale localization results from less isolated areas due to significantly enhanced long-range connections. Comparable impacts are observed when we adjust the strength of the FLN.

These diverse and somewhat paradoxical effects of various parameters highlight the complex interplay of factors that govern signal integration and propagation in the brain. Fully elucidating these intricate dynamics calls for more nuanced analyzes and modeling work, going beyond the scope of our current study, to fully unravel the underlying mechanisms of brain functionality.

Another important consideration relates to the anatomical connectivity data used: the tracer-derived FLN weights currently employed in our large-scale marmoset cortical model do not specify neurotransmitter identity of target neurons[25,26]. We therefore applied an identical FLN connectivity matrix to both excitatory (E) and inhibitory (I) neuronal populations within each cortical region, with their relative efficacies modulated by two global parameters, μ_{EE} and μ_{IE}. These global scaling parameters were carefully tuned to simultaneously satisfy crucial dynamical constraints–notably, the observed hierarchy of intrinsic timescales and robust inter-areal signal propagation–and were subsequently kept fixed throughout all simulations. While this simplification enables effective modeling of large-scale cortical dynamics, it neglects potential heterogeneity in cell-type specific projections. Future availability of cell-type resolved anatomical tracing data will refine the model by introducing projection-specific E/I targeting ratios instead of global scalar parameters.

While our model focuses exclusively on cortico-cortical connectivity, the cerebral cortex is not anatomically isolated – subcortical circuits (e.g., thalamus) and peripheral sensory pathways (retina, cochlea, spinal cord) impose important computational constraints on cortical activity. However, due to the lack of a marmoset-wide subcortical connectome at comparable resolution, our model necessarily focused on the corticocortical network, which can later be augmented with subcortical circuits as new data emerge. We anticipate that incorporating cortical-thalamo-cortical and peripheral pathways in future marmoset models will refine our present findings, particularly by enhancing model predictions related to intrinsic timescale patterns, signal propagation, and functional connectivity profiles. Incorporating such pathways represents a key direction for future work as compatible anatomical datasets become available.

Methods

Experimental data sources

This work analyzed two experimental datasets to estimate neuronal activity's time constants and signal propagation across cortical areas. The resting-state time constant was estimated from an ECoG dataset, gathered during an auditory task from a marmoset with a chronic implant in the left hemisphere[34]. The dataset features data from 96 uniformly placed electrodes throughout the hemisphere, gathered while the marmoset was in a resting state, under the influence of ketamine-based anesthesia (30 mg/kg i.m.). For the purpose of this study, we considered only the data collected prior to any auditory stimulus – ~15 ser trial – resulting in a cumulative total of 60 s of data compiled from four separate trials. We analyzed neural signals in 33 areas whose inter-areal connectivity has been measured in anatomical experiments[25,26]. The activity of these areas can be directly modeled, which enables us to compare experimental data with simulation results.

For the analysis of signal propagation across areas, we utilized an optogenetic ECoG dataset collected from the right hemisphere of an awake marmoset[37]. This dataset was gathered using a combination of 64 epidurally implanted electrodes and eight LEDs designated for optogenetic stimulation. We utilized recording data with a single LED stimulating approximately areas A4ab, A6DR, A6Va, AuCM, S2E, V3A, PE, and PG. Each recording trial incorporated a 200 ms pulse stimulus followed by a 2 s post stimulation interval, and the response was quantified by averaging the outcomes across a series of 50 trials.

For the intrinsic timescales during the awake resting state, we utilized the same optogenetic ECoG dataset for signal propagation analysis[37]. We specifically extracted the initial 5 s of recordings from the whole session – prior to any optogenetic stimulation–to obtain a resting–state segment free of task or laser effects. Nonetheless, due to the relatively short duration of awake-state recordings, we primarily used anesthetized-state data for subsequent analysis (e.g., comparisons with our model).

Estimation of the time constant of neural activity

We derived the time constants of neural activity during the resting state using a methodology based on PSD data[11]. This approach is especially beneficial when data length is short and the data contains oscillations and artifacts. The process entailed several stages. Initially, we computed the PSD using a variant of Welch's method[52] that involved 1-s long Hamming windows with 0.5-s overlap. For cases where multiple electrodes represented one area, we calculated the PSD individually for each electrode, subsequently taking the average as the PSD for that area.

Following this, we applied spectral parameterization[53] to decompose the PSD into a sum of Gaussians (representing temporal periodic terms) and a Lorentz function $L(f)$ (representing temporal aperiodic terms) given by the form

$$L(f) = \frac{A}{k + f^{\chi}}.$$

After fitting the data to determine the values of A, k, and χ, we identified the 'knee' frequency approximately as $f_k = k^{1/\chi}$. This frequency signifies the location where the PSD exhibits a 'knee' or bend. We then computed the corresponding timescale as $\tau = \frac{1}{2\pi f_k}$.

For the post-stimulus activity timescale, we fitted the response following peak activity (post-stimulus) using an exponential function

$$r(t) = ae^{-t/\tilde{\tau}}.$$

We determined the value of $\tilde{\tau}$ that provided the best fit as the time constant of the neural response in each cortical area.

Multi-regional cortical model architecture

We built the multi-regional marmoset cortical model using a set of ordinary differential equations, adapted from previous works of modeling macaque cortical network[1,33]. In the model, 55 areas from sensory to association cortex were included. Each cortical area was modeled with one excitatory and one inhibitory neuron group

governed by the following dynamics:

$$\tau_E \frac{d}{dt} r_E^i = -r_E^i + \beta_E \left[(1+\eta_E h_i) w_{EE} r_E^i - w_{EI} r_I^i + (1+\eta_E h_i) \mu_{EE} \sum_{j=1}^{N} FLN_{ij} r_E^j + I_{\text{ext,E}}^i \right]_+, \quad (1)$$

$$\tau_I \frac{d}{dt} r_I^i = -r_I^i + \beta_I \left[(1+\eta_I h_i) w_{IE} r_E^i - w_{II} r_I^i + (1+\eta_I h_i) \mu_{IE} \sum_{j=1}^{N} FLN_{ij} r_E^j + I_{\text{ext,I}}^i \right]_+. \quad (2)$$

In these equations, r_E^i and r_I^i represent the firing rates of the excitatory and inhibitory populations in area i, respectively, while τ_E and τ_I are the corresponding intrinsic time constants. w_{XY} symbolizes the coupling strength from Y population to X population within the area (X, Y could be E or I population). μ_{XE} represents the coupling strength of the inter-areal input from the excitatory population to the X population in a downstream cortical area, while FLN_{ij} signifies the FLN from area j to area i. The external input to the X population in area i is expressed as $I_{ext,X}^i$. We used a threshold linear function $f(x) = \beta[x]_+$ for the gain function for both E and I populations, with gain factors $\beta = \beta_E$ and β_I, respectively.

To complement our large-scale model that uses FLN to describe inter-areal connectivity, we additionally introduced a composite gradient of excitation, h. Because the FLN matrix is normalized per target area (each row sums to 1), it encodes only relative inter-areal connectivity but does not capture the area-wise differences in the absolute number of synapse inputs received by each target area. Anatomical evidence indicates that neurons in higher-order association cortex receive more inputs per cell than those in early sensory areas. For instance, dendritic spine counts increase systematically from sensory to association areas[26]. Furthermore, a uniform ~80%/20% division of local versus long-range inputs across areas[54] implies that higher-order areas inherently possess greater numbers of both local and inter-areal synapses. Thus, neurons in association cortex receive a larger overall drive than those in lower areas. To account for this gradient, we define a composite gradient of excitation h as an area-specific scaling factor applied to all synaptic weights, effectively representing the increasing synaptic density in higher cortical areas while preserving the empirically measured FLN connectivity pattern. Within our model, h_i is a factor scaling both local (intra-areal) and long-range (inter-areal) excitatory inputs and varies across different areas. The quantitative estimation of h_i is detailed in the subsequent subsection. The scaling factor η_X governs the slope of the composite gradient on the X population.

Adapted from a previous experimental study[55], we set $\tau_E = 20ms$, $\tau_I = 10ms$, $\beta_E = 0.066Hz/pA$, $\beta_I = 0.351Hz/pA$, $\eta_E = 0.685$, $\eta_I = 0.76$, $w_{EE} = 24.4pA/Hz$, $w_{EI} = 19.7pA/Hz$, $w_{IE} = 11.66pA/Hz$, $w_{II} = 12.5pA/Hz$, $\mu_{EE} = 67.4pA/Hz$, $\mu_{IE} = 49.81pA/Hz$.

Incorporation of axonal conduction delays

We also extended the multi-area rate-based model to include explicit axonal conduction delays on all connections, both inter-areal and intra-areal for some studies. Inter-areal transmission delays, τ_{ij}, were defined as proportional to the anatomical distance between the source area j and the target area i. Specifically, we set $\tau_{ij} = d_{ij}/v_{ax}$, where d_{ij} is the white-matter tract length between areas i and j[25] and $v_{ax} = 3.5$ m/s is the assumed axonal conduction velocity. All intra-areal (local) recurrent projections were assigned a fixed delay of 2 ms. These parameter values align with those used in previous large-scale modeling studies of macaque cerebral cortex[33], thereby ensuring biologically plausible transmission latencies consistent with existing literature.

Delays were implemented by introducing a time shift in the firing-rate equations (Eqs. (1) and (2)) for each synaptic input. Specifically, any synaptic input from population β in area j to population α in area i was applied with a time offset corresponding to the assigned delay. For inter-areal connections ($i \neq j$), the presynaptic activity from population β at time $t-\tau_{ij}$ was used when computing input to the postsynaptic population α at time t. Similarly, for local recurrent connections ($i = j$), population activity at $t-2$ ms was used in the coupling terms. This delayed-input mechanism was integrated the existing rate model dynamics without modifying any other parameters. The complete formula is as follows:

$$\tau_E \frac{d}{dt} r_E^i(t) = -r_E^i(t) + \beta_E \left[(1+\eta_E h_i) w_{EE} r_E^i(t-2) - w_{EI} r_I^i(t-2) + (1+\eta_E h_i) \mu_{EE} \sum_{j=1}^{N} FLN_{ij} r_E^j(t-\tau_{ij}) + I_{\text{ext,E}}^i(t) \right]_+, \quad (3)$$

$$\tau_I \frac{d}{dt} r_I^i(t) = -r_I^i(t) + \beta_I \left[(1+\eta_I h_i) w_{IE} r_E^i(t-2) - w_{II} r_I^i(t-2) + (1+\eta_I h_i) \mu_{IE} \sum_{j=1}^{N} FLN_{ij} r_E^j(t-\tau_{ij}) + I_{\text{ext,I}}^i(t) \right]_+. \quad (4)$$

Importantly, introducing these biologically realistic conduction delays did not substantially change the primary results of the model: the global inter-areal sigal propagation patterns and the intrinsic timescale hierarchy remained robust and unchanged (Supplementary Fig. S8).

Estimation of macroscopic gradient of excitation

We incorporated the composite gradient of excitation h_i in the model to be consistent with the experimental findings related to the gradient of timescale across areas and the structural hierarchy derived from the fraction of supragranular labeled neurons (SLN) as reported in ref. 26. As the model includes more areas (55 areas) than those recorded in the ECoG experiment (33 areas), the fitting was performed in two steps: firstly, we determined the composite gradient value of the 33 areas whose activity data and structural hierarchy data were both available. Secondly, we calculated the values of h_i for the rest areas based on the structural hierarchy and the values of h_i for the 33 areas obtained in the first step.

For the 33 areas whose timescale and structural hierarchy were both available, we used the following objective function that combined the similarity between the excitation composite gradient parameter h_i with the structural hierarchy $h_{i,exp}$ determined by SLN and the timescale $\tau_{i,exp}$ derived from neural signals, i.e.,

$$\mathcal{L}(\mathbf{h}) = \text{Corr}\left(\tau_{exp}, 1/(1-\mathbf{h})\right) + \lambda \,\text{Corr}\left(\mathbf{h}_{exp}, \mathbf{h}\right)$$

where $\mathbf{h}$,$\mathbf{h}_{exp}$ and τ_{exp} are vectors, and λ is a hyper-parameter that determines the preference for the gradient to be closer to the timescale or the experimental hierarchy (chosen as 1 in this work). The Corr(a, b) is the Pearson's correlation coefficient between a and b. We assessed the similarity with the structural hierarchy $\mathbf{h}_{exp}$ by measuring the correlation coefficient, and evaluated the similarity with the timescale τ_{exp} by calculating the correlation coefficient between $1/(1-\mathbf{h})$ and the experimentally measured timescale. We made this choice based on a mathematical analysis showing that $1-\mathbf{h}$ is proportional to the inverse of the time constant of neural activity when the multiple brain areas in the system are decoupled (details provided in Supporting Information). To obtain the values of the composite gradient, we solved the optimization problem presented by the objective function:

$$\mathbf{h}^* = \arg\max_{\mathbf{h}} \mathcal{L}(\mathbf{h}). \quad (5)$$

For areas whose timescale data could not be obtained from experiments (no electrode is placed in these areas), we determined their composite gradient h_i as a weighted average of the gradients of the 33

areas whose gradient h_j have been estimated in the first step. The weight was based on the similarity between structural hierarchy of two areas:

$$h_i^* = \sum_{j=1}^{33} h_j^* e^{-d_{ij}^2/\sigma^2}$$

where $d_{ij} = |h_{i,exp} - h_{j,exp}|$ is the difference of structural hierarchy for area i, j and $\sigma = 0.05$.

Simulation scenarios

We examined multiple simulation scenarios in the study. The scenarios encompassed a range of parameter configurations and manipulations of the network connectivity. For scenarios related to the change of gradient, we removed gradients (Figs. 4a, d, and 6a) by setting all $h_i = 0$. Furthermore, we manipulated the slope of the composite gradients by scaling with a factor γ (Figs. 4b, and 6b), leading to $h_i^{(new)} = \gamma h_i$ or by interpolating between the average gradient of all areas $\bar{h}$ and the gradient h_i (Fig. 6b)

$$h_i^{(new)} = (1-\gamma) * \bar{h} + \gamma * h_i, 0 \le \gamma \le 1.$$

For Fig. 6c, the gradient slope γ is set to 0.

In scenarios involving the change of network connectivity FLNs, we devised a condition devoid of any feedback loops by assigning zero to all FLN entries where the connection has a smaller fraction of neurons in a projection originating from the supragranular layers of the source area (Fig. 7c), namely $FLN_{ij} = 0$, for all $SLN_{ij} < 0.5$. For Fig. 5c–f, we shuffled the FLN by randomly permuting its entries 1000 times to obtain the distribution of the corresponding measures.

Regarding other parameter modifications, we disrupted the E-I balance by augmenting w_{EI} by 10% (Fig. 5a). For Fig. 8b–d, we set $\mu_{IE} = 24.91, 37.36, 49.81$ pA/Hz, respectively and computed the corresponding upper bound μ_{EE}^* as 34.03, 50.68, 67.40 pA/Hz such that the system remains stable. μ_{EE} was varied as $\lambda\mu_{EE}^*$ with λ ranging from 0.95, 0.97, 0.975 to 1 for each respective μ_{IE} setting. For Fig. S4, we varied the value of μ_{EE} within the range from 64 to 70.

Metrics for timescale localization

We employed two quantitative measures to describe timescale localization across the whole neocortex. The first is the IPR, which was originally introduced in quantum mechanics and solid-state physics. For a normalized eigenvector $\mathbf{v}$, its IPR is defined as follows:

$$\mathrm{IPR}(\mathbf{v}) = \sum_{j=1}^{N} |v_j|^4$$

where v_j is the jth element of $\mathbf{v}$. The IPR for the eigenvector matrix is computed as the average IPR across each column (eigenvector) in the matrix.

Furthermore, we introduced an additional metric for spatial localization of eigenvector $\mathbf{v}$ (Luis Carlos Garcia and Xiao-Jing Wang, see ref. 38):

$$\theta(\mathbf{v}) = \sum_{i,j=1}^{N} |v_i|^4 |v_j|^4 e^{-d_{ij}/\bar{d}}.$$

Here, d_{ij} represents the distance between a pair of areas i and j, which, in our context, denotes the physical distances between two areas in the marmoset neocortex; $\bar{d}$ signifies the average distance across all pairs.

Reporting summary

Further information on research design is available in the Nature Portfolio Reporting Summary linked to this article.

Data availability

All data used in this study are publicly available from the Brain/MINDS project datasets[34,37].

Code availability

The source code and scripts used for simulation, analysis and figure generation are openly accessible on GitHub (https://github.com/GuanchunLi/Marmoset_Cortex_Model/), archived in https://doi.org/10.5281/zenodo.17188863[51].

References

1. Chaudhuri, R., Knoblauch, K., Gariel, Marie-Alice, Kennedy, H. & Wang, Xiao-Jing. A large-scale circuit mechanism for hierarchical dynamical processing in the primate cortex. *Neuron* **88**, 419–431 (2015).
2. Runyan, C. A., Piasini, E., Panzeri, S. & Harvey, C. D. Distinct timescales of population coding across cortex. *Nature* **548**, 92–96 (2017).
3. Siegle, J. H. et al. Survey of spiking in the mouse visual system reveals functional hierarchy. *Nature* **592**, 86–92 (2021).
4. Ogawa, T. & Komatsu, H. Differential temporal storage capacity in the baseline activity of neurons in macaque frontal eye field and area v4. *J. Neurophysiol.* **103**, 2433–2445 (2010).
5. Murray, J. D. et al. A hierarchy of intrinsic timescales across primate cortex. *Nat. Neurosci.* **17**, 1661–1663 (2014).
6. Hasson, U., Yang, E., Vallines, I., Heeger, D. J. & Rubin, N. A hierarchy of temporal receptive windows in human cortex. *J. Neurosci.* **28**, 2539–2550 (2008).
7. Honey, C. J. et al. Slow cortical dynamics and the accumulation of information over long timescales. *Neuron* **76**, 423–434 (2012).
8. Yeshurun, Y., Nguyen, M. & Hasson, U. Amplification of local changes along the timescale processing hierarchy. *Proc. Natl. Acad. Sci. USA* **114**, 9475–9480 (2017).
9. Raut, R. V., Snyder, A. Z. & Raichle, M. E. Hierarchical dynamics as a macroscopic organizing principle of the human brain. *Proc. Natl. Acad. Sci. USA* **117**, 20890–20897 (2020).
10. Shafiei, G. et al. Topographic gradients of intrinsic dynamics across neocortex. *eLife* **9**, e62116 (2020).
11. Gao, R., van den Brink, R. L., Pfeffer, T. & Voytek, B. Neuronal timescales are functionally dynamic and shaped by cortical microarchitecture. *eLife* **9**, e61277 (2020).
12. Elston, G. N. Specialization of the neocortical pyramidal cell during primate evolution. in *Evolution of Nervous Systems*, 191–242 (Elsevier, 2007).
13. Elston, G. N., Tweedale, R. & Rosa, MarcelloG. P. Cellular heterogeneity in cerebral cortex: a study of the morphology of pyramidal neurones in visual areas of the marmoset monkey. *J. Comp. Neurol.* **415**, 33–51 (1999).
14. Kim, Y. et al. Brain-wide maps reveal stereotyped cell-type-based cortical architecture and subcortical sexual dimorphism. *Cell* **171**, 456–469 (2017).
15. Fulcher, B. D., Murray, J. D., Zerbi, V. & Wang, Xiao-Jing Multimodal gradients across mouse cortex. *Proc. Natl. Acad. Sci. USA* **116**, 4689–4695 (2019).
16. Froudist-Walsh, S. et al. Gradients of neurotransmitter receptor expression in the macaque cortex. *Nat. Neurosci.* **26**, 1281–1294 (2023).
17. Wang, Xiao-Jing Macroscopic gradients of synaptic excitation and inhibition in the neocortex. *Nat. Rev. Neurosci.* **21**, 169–178 (2020).
18. Oh, SeungWook et al. A mesoscale connectome of the mouse brain. *Nature* **508**, 207–214 (2014).
19. Zingg, B. et al. Neural networks of the mouse neocortex. *Cell* **156**, 1096–1111 (2014).
20. Gămănuț, R. ăzvan et al. The mouse cortical connectome, characterized by an ultra-dense cortical graph, maintains specificity by distinct connectivity profiles. *Neuron* **97**, 698–715 (2018).

21. Harris, J. A. et al. Hierarchical organization of cortical and thalamic connectivity. *Nature* **575**, 195–202 (2019).
22. Kennedy, H., Knoblauch, K. & Toroczkai, Zoltán. Why data coherence and quality is critical for understanding interareal cortical networks. *NeuroImage* **80**, 37–45 (2013).
23. Markov, N. T. et al. A weighted and directed interareal connectivity matrix for macaque cerebral cortex. *Cereb. Cortex* **24**, 17–36 (2014).
24. Markov, N. T. et al. Anatomy of hierarchy: feedforward and feedback pathways in macaque visual cortex. *J. Comp. Neurol.* **522**, 225–259 (2014).
25. Majka, P. et al. Open access resource for cellular-resolution analyses of corticocortical connectivity in the marmoset monkey. *Nat. Commun.* **11**, 1133 (2020).
26. Theodoni, P. et al. Structural attributes and principles of the neocortical connectome in the marmoset monkey. *Cereb. Cortex* **32**, 15–28 (2022).
27. Felleman, D. J. & Van Essen, D. C. Distributed hierarchical processing in the primate cerebral cortex. *Cereb. Cortex* **1**, 1–47 (1991).
28. Stephan, K. E. et al. Advanced database methodology for the collation of connectivity data on the macaque brain (cocomac). *Philos. Trans. R. Soc. Lond. Ser. B* **356**, 1159–1186 (2001).
29. Ercsey-Ravasz, M. ária et al. A predictive network model of cerebral cortical connectivity based on a distance rule. *Neuron* **80**, 184–197(2013).
30. Horvát, S. et al. Spatial embedding and wiring cost constrain the functional layout of the cortical network of rodents and primates. *PLoS Biol.* **14**, e1002512 (2016).
31. Li, S. & Wang, Xiao-Jing Hierarchical timescales in the neocortex: Mathematical mechanism and biological insights. *Proc. Natl. Acad. Sci. USA* **119**, e2110274119 (2022).
32. Vogels, T. P. & Abbott, L. F. Gating multiple signals through detailed balance of excitation and inhibition in spiking networks. *Nat. Neurosci.* **12**, 483–491 (2009).
33. Joglekar, M. R., Mejias, J. F., Yang, GuangyuRobert & Wang, Xiao-Jing. Inter-areal balanced amplification enhances signal propagation in a large-scale circuit model of the primate cortex. *Neuron* **98**, 222–234 (2018).
34. Komatsu, M. & Ichinohe, N. Brain/minds marmoset brain ecog auditory dataset 01 (dataid: 4924).
35. Nakae, K. et al. Brain/minds marmoset brain ecog annotations of electrodes (dataid: 4958).
36. Chaudhuri, R., He, B. J. & Wang, Xiao-Jing Random recurrent networks near criticality capture the broadband power distribution of human ecog dynamics. *Cereb. Cortex* **28**, 3610–3622 (2018).
37. Komatsu, M., Sugano, E., Tomita, H., and Fujii, N. Brain/minds marmoset optogenetics dataset 01 (dataid: 3718).
38. Wang, X.-J. *Theoretical Neuroscience: Understanding Cognition* (CRC Press, Boca Raton, 2025).
39. Deco, G. et al. Resting-state functional connectivity emerges from structurally and dynamically shaped slow linear fluctuations. *J. Neurosci.* **33**, 11239–11252 (2013).
40. Hayashi, T. et al. The nonhuman primate neuroimaging and neuroanatomy project. *NeuroImage* **229**, 117726 (2021).
41. Thomas Yeo, B.T. et al. The organization of the human cerebral cortex estimated by intrinsic functional connectivity. *J. Neurophysiol.* **106** 1125–1165 (2011).
42. Fotiadis, P. et al. Myelination and excitation-inhibition balance synergistically shape structure-function coupling across the human cortex. *Nat. Commun.* **14**, 6115 (2023).
43. Fotiadis, P. et al. Structure–function coupling in macroscale human brain networks. *Nat. Rev. Neurosci.* **25**, 688–704 (2024).
44. Petermann, T. et al. Spontaneous cortical activity in awake monkeys composed of neuronal avalanches. *Proc. Natl. Acad. Sci. USA* **106**, 15921–15926 (2009).
45. Priesemann, V. et al. Spike avalanches in vivo suggest a driven, slightly subcritical brain state. *Front. Syst. Neurosci.* **8**, 108 (2014).
46. Wilting, J. & Priesemann, V. Inferring collective dynamical states from widely unobserved systems. *Nat. Commun.* **9**, 2325 (2018).
47. Fagerholm, E. D. et al. Cascades and cognitive state: focused attention incurs subcritical dynamics. *J. Neurosci.* **35**, 4626–4634 (2015).
48. Munn, B. R. et al. Neuronal connected burst cascades bridge macroscale adaptive signatures across arousal states. *Nat. Commun.* **14**, 6846 (2023).
49. Maschke, C. et al. Critical dynamics in spontaneous EEG predict anesthetic-induced loss of consciousness and perturbational complexity. *Commun. Biol.* **7**, 946 (2024).
50. Moretti, P. & Muñoz, M. A. Griffiths phases and the stretching of criticality in brain networks. *Nat. Commun.* **4**, 2521 (2013).
51. Li, G., Li, S. & Wang, X.-J. A hierarchy of time constants and reliable signal propagation in the marmoset cerebral cortex (code repository). https://doi.org/10.5281/zenodo.17188863 (2025).
52. Izhikevich, L., Gao, R., Peterson, E. & Voytek, B. Measuring the average power of neural oscillations. Preprint at *bioRxiv* https://www.biorxiv.org/content/10.1101/441626v2.full (2018).
53. Donoghue, T. et al. Parameterizing neural power spectra into periodic and aperiodic components. *Nat. Neurosci.* **23**, 1655–1665 (2020).
54. Markov, N. T. et al. Weight consistency specifies regularities of macaque cortical networks. *Cereb. Cortex* **21**, 1254–1272 (2011).
55. Binzegger, T., Douglas, R. J. & Martin, KevanA. C. Topology and dynamics of the canonical circuit of cat V1. *Neural Netw.* **22**, 1071–1078 (2009).

Acknowledgements

We thank Cirong Liu for suggestions on area identification of the optogenetic ECoG public dataset, and thank Marcello Rosa and Sean Froudist-Walsh for help categorize marmoset brain areas into seven subnetworks. This work is supported by National Key R&D Program of China 2023YFF1204200, National Natural Science Foundation of China Grant 12271361, 12250710674, Science and Technology Commission of Shanghai Municipality Grant No. 24JS2810400 and the Student Innovation Center at Shanghai Jiao Tong University (S.L.), James Simons Foundation Grant NC-GB-CULM-00003138 (X.-J.W.).

Author contributions

G.L., S.L., and X.-J.W. designed the research, had regular discussions throughout the project, and wrote the manuscript. G.L. and S.L. performed the computational research.

Competing interests

The authors declare no competing interests.

Additional information

Supplementary information The online version contains supplementary material available at https://doi.org/10.1038/s41467-025-66699-4.

Correspondence and requests for materials should be addressed to Songting Li or Xiao-Jing Wang.

Peer review information *Nature Communications* thanks the anonymous reviewer(s) for their contribution to the peer review of this work. A peer review file is available.